Navier-Stokes Solutions for Vortical Flows over a Tangent-Ogive Cylinder

Peter-M. Hartwich*
Vigyan, Inc., Hampton, Virginia
and
R. M. Hall†
NASA Langley Research Center, Hampton, Virginia

Reynolds number (Re) effects on low-speed vortical flows over 3.5-caliber, tangent-ogive cylinders at two angles of attack ($\alpha = 20$ and 30 deg) are computationally assessed for $Re_D = 0.2$–3 million (D: maximum diameter). The flowfield results are steady-state solution to the three-dimensional, incompressible Navier-Stokes equations in their thin-layer approximation. Using a properly modified algebraic turbulence model, the numerical results are in good to excellent agreement with experiments. For the first time, a crossflow separation pattern, which consists of a laminar separation bubble with a subsequent transition in the separating shear layer that forms a primary vortex, has been modeled. The discussion of the computed results includes a rigorous assessment of the effects of gridding and of turbulence modeling.

Nomenclature

A,B,C = Jacobians $\partial E/\partial Q$, $\partial F/\partial Q$, and $\partial G/\partial Q$
a,b,c = metric coefficient like ξ_x, ξ_y, and ξ_z
C_{cp} = constant in turbulence model
C_p = pressure coefficient
$C_{p,t}$ = total pressure coefficient
C_{wk} = constant in turbulence model
CFL = Courant-Friedrich-Lewy number
D = maximum body diameter (= caliber)
d = local-body diameter
E,F,G = flux vectors
F = function in the turbulence model
F_{Kleb} = Klebanoff factor
F_{wake} = wake function
h = representative spatial step size
I = identity matrix
J = Jacobian of the coordinate transformation
K = Clauser constant
k = von Kármán constant in turbulence model
L = matrix whose rows are left eigenvectors
l = length
M = matrix in implicit operators
p = nondimensional static pressure
Q = state vector
R = matrix whose columns are right eigenvectors
Re = Reynolds number
RES = residual
r = ratio of two consecutive changes in characteristic variables
S = artificial speed of sound
U,V,W = dimensional contravariant velocity components
u,v,w = Cartesian velocity components
α = angle of attack
β = amount of artificial compressibility
Δ = difference operator
δ = difference operator
ζ,ξ,η = curvilinear coordinates
Λ = diagonal matrix with eigenvalues as entries
λ = eigenvalues
ρ = density
τ = time-step size
ϕ = limiter

Subscripts

D = maximum diameter
i,j,k = indices in ζ,ξ,η directions in regular computational domain
ℓ = i, j, or k
m = mth component of some vector
v = denotes viscous shear fluxes
x,y,z = differentiation in x, y, and z directions
ζ,ξ,η = differentiation in ζ, ξ, and η directions
∞ = freestream values

Superscripts

n = time level
T = transpose of a matrix
$+$ = turbulent quantities
$*$ = dimensional

Received Nov. 22, 1988; revision received July 10, 1989.

*Research Scientist. Member AIAA.
†Senior Research Engineer. Associate Fellow AIAA.

I. Introduction

VORTICAL flows over slender forebody-type configurations have stirred the minds of experimentalists and numericists alike.[1] Even though the body geometries are simple (e.g., hemisphere cylinder, tangent ogive, etc.), the flows around them are intricate[2,3] as illustrated by the sketches in Fig. 1. There can be either a fully laminar (LS) or a fully turbulent (TS) crossflow separation pattern, which may or may not include a secondary vortex. At intermediate values of Reynolds number, the most complex crossflow separation pattern (TRS) occurs: a laminar three-dimensional, bubble-type structure in the equatorial regime followed by transition in the separated shear layer. Moreover, all of these separation patterns can be observed for constant values for α and Re_D. At the apex, where the local body diameter d is quite small, the laminar separation pattern occurs. Further back, as the local diameter grows, first the TRS pattern can appear and then the TS pattern if Re_D is sufficiently large.

Traditional analytical and empirical analyses[4,5] have attained some success in predicting the gross properties associ-

B	bubble-type region
LS	laminar crossflow separation
R	reattachment
SS	secondary separation
TRS	transitional crossflow separation
TS	turbulent crossflow separation

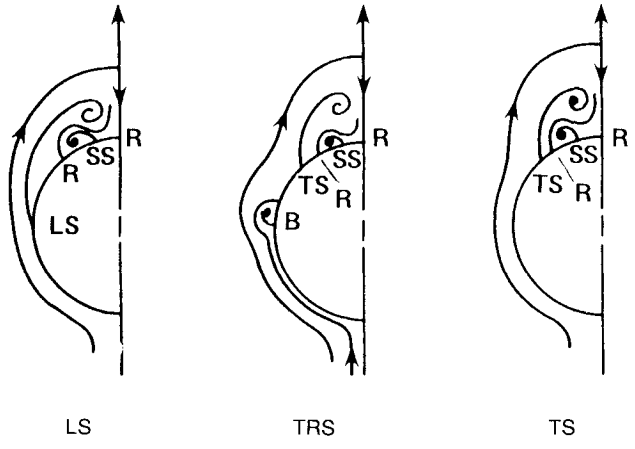

Fig. 1 Keener's[2] sketches of crossflow separation patterns for a 3.5-caliber, tangent-ogive cylinder.

ated with vortical flows past forebodies, but they have been unable to describe the physical details. Starting with the work by Pulliam and Steger,[6] several attempts have been made to predict such flows as solutions to the Euler and Navier-Stokes equations. The Euler equations are the simplest subset of the Navier-Stokes equations that properly account for rotational effects, which, for shockless flows, can only be due to separation. Neglecting the special case of forebodies with sharp edges (e.g., chines), separation has to be modeled by imposing Kutta-Joukowski-type conditions[7,8] along the separation lines. That precludes flowfield calculations without an experimental data base. In contrast to the Euler equations, the Navier-Stokes equations can accurately capture the details of flow separations without any such empirical separation modeling. Even proper simulation of transition and turbulence—problems which the Navier-Stokes equations share with other mathematical models—is attainable by rather small modifications to existing, relatively simple turbulence models, for at least certain classes of flows with massive crossflow separation.[9,10]

In the present study, the effects of Reynolds number and angle of attack on vortical flows over a 3.5-caliber, tangent-ogive cylinder are examined using FMC1, a proven, high-resolution, upwind solver for the three-dimensional, incompressible Navier-Stokes equations in their thin-layer approximation.[10-12] This incompressible solver was chosen since comparable experimental studies have been focused in low-speed flows with $M<0.3$.[1,2,13,14] For this speed regime, incompressible flow solvers offer the advantage of improved efficiency and, sometimes, higher accuracy.[11,12,15] The governing equations are given first and followed by a brief review of the salient, numerical ingredients of the flow solver. A rational modification of the algebraic turbulence model by Baldwin and Lomax[16] is presented that is consistent with the physics of the flow and which extends the applicability of FMC1 to forebody flows with massive crossflow separation. After some comments on the implementation of the boundary conditions, computed flowfield results are discussed for two angles of attack, $\alpha = 20$ and 30 deg and three Reynolds numbers, $Re_D = 0.2$, 0.8, and 3 million, which includes the assessment of gridding effects and of transition/turbulence modeling on the computed flowfield results.

II. Differential Equations and Numerical Method

The three-dimensional, incompressible Navier-Stokes equations are solved in their thin-layer approximation for several reasons: 1) the viscous shear fluxes can be treated fully implicitly, 2) the memory available in today's computers permits resolution of the viscous-length scales only normal to a body surface, 3) algebraic turbulence models depend only on the local normal velocity profiles,[9,16] and 4) as in other numerical studies,[9,12,17] the steady-state solutions to the thin layer and to the complete Navier-Stokes equations are found to be equivalent. Employing Chorin's[18] artificial compressibility concept, and assuming a reference length l_{ref} and a reference speed v_∞, the nondimensional governing equations in generalized curvilinear coordinates are

$$\partial_t(Q/J) + \partial_\xi E + \partial_\xi F + \partial_\eta(G - G_v) = 0 \tag{1}$$

with

$$Q = (p,u,v,w)^T$$

$$E = (\beta U,\ uU + \zeta_x p,\ vU + \zeta_y p,\ wU + \zeta_z p)^T$$

$$F = (\beta V,\ uV + \xi_x p,\ vV + \xi_y p,\ wV + \xi_z p)^T$$

$$G = (\beta W,\ uW + \eta_x p,\ vW + \eta_y p,\ wW + \eta_z p)^T$$

$$G_v = (Re \cdot J)^{-1} \begin{bmatrix} 0 \\ \psi_1 u_\eta + \psi_2 \eta_x \\ \psi_1 v_\eta + \psi_2 \eta_y \\ \psi_1 w_\eta + \psi_2 \eta_z \end{bmatrix}$$

where

$$\psi_1 = \eta_x^2 + \eta_y^2 + \eta_z^2 \qquad \psi_2 = (\eta_x u_\eta + \eta_y v_\eta + \eta_z w_\eta)/3$$

$$U = \zeta_x u + \zeta_y v + \zeta_z w \qquad V = \xi_x u + \xi_y v + \xi_z w$$

$$W = \eta_x u + \eta_y v + \eta_z w$$

$$J^{-1} = x_\xi(y_\xi z_\eta - y_\eta z_\xi) + x_\xi(y_\eta z_\zeta - y_\zeta z_\eta) + x_\eta(y_\zeta z_\xi - y_\xi z_\zeta)$$

$$\zeta_x = (y_\xi z_\eta - y_\eta z_\xi) \qquad \zeta_y = -(x_\xi z_\eta - x_\eta z_\xi)$$

$$\zeta_z = (x_\xi y_\eta - x_\eta y_\xi) \qquad \xi_x = (y_\eta z_\zeta - y_\zeta z_\eta)$$

$$\xi_y = -(x_\eta z_\zeta - x_\zeta z_\eta) \qquad \xi_z = (x_\eta y_\zeta - x_\zeta y_\eta)$$

$$\eta_x = (y_\zeta z_\xi - y_\xi z_\zeta) \qquad \eta_y = -(x_\zeta z_\xi - x_\xi z_\zeta)$$

$$\eta_z = (x_\zeta y_\xi - x_\xi y_\zeta)$$

and

$$x,y,z = x^*,y^*,z^*/\ell_{\text{ref}} \qquad t = t^*\ell_{\text{ref}}/v_\infty$$

$$u,v,w = u^*,v^*,w^*/v_\infty \qquad p = (p^* - p_\infty)/\rho v_\infty^2 = C_p/2$$

Steady-state solutions to Eq. (1) recover the governing equations for steady, incompressible flows. The parameter β determines how closely the continuity equation is coupled with the momentum equations. By analysis[11,12,15] and by previous[10-12] and present experience, $\beta = 1$ has been found to be a suitable choice for steady-state calculations.

For the upwinding of the inviscid fluxes and for the implicit algorithm, we will need the Jacobians for the inviscid fluxes E, F, and G. Defining

$$A = \partial E/Q \quad B = \partial F/\partial Q \quad C = \partial G/\partial Q \tag{2}$$

the Jacobians are given by

$$A,\ B,\ \text{or}\ C = \begin{bmatrix} 0 & a\beta & b\beta & c\beta \\ a & au+\theta & bu & cu \\ b & av & bv+\theta & cv \\ c & aw & bw & cw+\theta \end{bmatrix} \tag{3}$$

where $\theta = U$, V, or W, and $a = \zeta_x$, ξ_x, or η_x, etc. The Jacobians comprised in Eq. (3) have a complete set of real eigenvalues[11,12,15]

$$\Lambda = \text{diag}\ (\lambda_1,\lambda_2,\lambda_3,\lambda_4) = \text{diag}\ (\theta - S, \theta + S, \theta, \theta) \tag{4}$$

where $S = [\theta^2 + \beta\ (a^2 + b^2 + c^2)]^{1/2}$ and diag = diagonal matrix. The matrices A, B, and C can be split according to the sign of their real eigenvalues as, for instance,

$$A^-_{i+1/2} = (R\Lambda^- L)_{i+1/2} \text{ and } A^+_{i-1/2} = (R\Lambda^+ L)_{i-1/2} \tag{5}$$

with $\Lambda^\pm = (|\Lambda| \pm \Lambda)/2$. The columns of R and the rows of L give the linearly independent right and left eigenvectors, respectively, and they should, for the sake of simplicity, be defined as an orthonormal set as $RL = I$. The analytical expressions for the eigenvectors R and L are readily found in Refs. 11 and 12. Using a second-order accurate-total variation diminishing (TVD)-like discretization[11-12] of the inviscid fluxes yields, for instance, the following backward and forward difference formulas for $E^\mp_{i\pm 1/2}$

$$E^\mp_{i\pm 1/2} = R_{i\pm 1/2}\left\{\Lambda^\mp_{i\pm 1/2}\ [I - 0.5(\Phi^\mp_{i\pm 1} - \Phi^\pm_i)]\right\}\Delta_{i\pm 1/2} W \tag{6}$$

where

$$\Phi_i = \text{diag}\ (\phi_1^\pm,\phi_2^\pm,\phi_3^\pm,\phi_4^\pm)_i$$

and

$$\Delta_{i\pm 1/2} W = L_{i\pm 1/2}\Delta_{i\pm 1/2} Q$$

with

$$\Delta_{i-1/2}(\ ) = (\ )_i - (\ )_{i-1}$$

The modified min-mod limiters[12] are defined as

$$\phi^\pm_{m,i} = \max\left[0,\ \min\ (1, r^\pm_{m,i}, 2r^\mp_{m,i\pm 1})\right] \tag{7}$$

with

$$r^\pm_{m,i} = (\Delta_{i-1/2} w^n_m / \Delta_{i+1/2} w^n_m)^{\pm 1} \text{ for } \Delta_{i\pm 1/2} w^n_m \neq 0$$
$$= 0 \qquad \text{for } \Delta_{i\pm 1/2} w^n_m = 0 \tag{8}$$

Second-order central differencing is applied to the viscous shear fluxes, which, for example, gives

$$(Re \cdot J)^{-1}_{k+1/2}\ (\psi_{1,k+1/2}\Delta_{k+1/2}\ u + \psi_{2,k+1/2}\ \eta_{x,k+1/2}) \tag{9}$$

and

$$\psi_{2,k+1/2} = (\eta_{x,k+1/2}\ \Delta_{k+1/2}\ u + \eta_{y,k+1/2}\ \Delta_{k+1/2}\ v + n_{z,k+1/2}\ \Delta_{k+1/2}\ w)/3$$

for the second term in G_v in Eq. (1). The metric quantities at full points are calculated from a freestream preserving averaging procedure[11,12]; their values at half points are arithmetic averages of their values at the adjacent full points.

The thin-layer approximation to the Navier-Stokes equations allows for a fully implicit treatment of the viscous shear flux G_v.[19] Upon applying Steger's[19] arguments, we derive a "viscous" coefficient matrix C_v as

$$C_v = (Re \cdot J)^{-1} \begin{bmatrix} 0 & 0 & 0 & 0 \\ 0 & z_{22} & z_{32} & z_{42} \\ 0 & z_{32} & z_{33} & z_{43} \\ 0 & z_{42} & z_{43} & z_{44} \end{bmatrix} \tag{10}$$

with

$$z_{22} = 4\eta_x^2/3 + \eta_y^2 + \eta_z^2 \qquad z_{33} = \eta_x^2 + 4\eta_y^2/3 + \eta_z^2$$
$$z_{32} = \eta_x\eta_y/3 \qquad z_{43} = \eta_y\eta_z/3$$
$$z_{42} = \eta_x\eta_z/3 \qquad z_{44} = \eta_x^2 + \eta_y^2 + 4\eta_z^2/3$$

In a hybrid formulation, the implicit finite-difference algorithm to solve Eq. (1) is written as

$$[M - B^-_{j+1/2}\ \Delta_{j+1/2} + B^+_{j-1/2}\Delta_{j-1/2}]^n\ [M^{-1}]^n$$
$$\times [M - (C^- + C_v)_{k+1/2}\Delta_{k+1/2} + (C^+ + C_v)_{k-1/2}$$
$$\times \Delta_{k-1/2}]^n\ \Delta Q^n = -\text{RES}\ (Q^n, Q^{n+1}) \tag{11}$$

with

$$M = (I/\tau J) + A^-_{1+1/2} + A^+_{i-1/2}$$

The algorithm in Eq. (11) combines approximate factorization (AF) in crossplanes with a symmetric, planar Gauss-Seidel relaxation in the ζ direction. The residual RES (Q^n, Q^{n+1}) consists of second-order accurate approximations to the spatial derivatives in Eq. (1), and it is nonlinearly updated during a forward or backward sweep in ζ direction. The steady-state solutions are independent of the time step size τ due to the delta formulation in Eq. (11). Second-order central differences for the viscous terms and first-order, one-sided differences for the inviscid fluxes are used for the formulation of the left side of Eq. (11).

III. Transition and Turbulence Modeling

Algebraic turbulence models have been chosen 1) because of their simplicity and 2) because they already proved to be easily extendable to handle turbulent flows with massive crossflow separation.[9,10] The two-layer, zero-equation model by Baldwin and Lomax[16] is applied to attached turbulent flows. To introduce the Baldwin-Lomax model in a nondimensional notation, we write the effective Reynolds number in Eq. (1) as

$$Re^{-1} = Re^{-1}_{\text{lam}} + Re^{-1}_{\text{turb}} \tag{12}$$

$$Re^{-1}_{\text{turb}} = \begin{cases} (Re^{-1}_{\text{turb}})_{\text{inner}}, & y \leq y_{\text{crossover}} \\ (Re^{-1}_{\text{turb}})_{\text{outer}}, & y > y_{\text{crossover}} \end{cases} \tag{13}$$

Here, y is the local distance normal to the body surface, and $y_{\text{crossover}}$ is the smallest value of y for which $(Re^{-1}_{\text{turb}})_{\text{inner}} = (Re^{-1}_{\text{turb}})_{\text{outer}}$. In the inner region

$$(Re^{-1}_{\text{turb}})_{\text{inner}} = \ell^2 |\omega| \tag{14}$$

where

$$\ell = ky\{1 - \exp\ [-(y^+/A^+)]\} \tag{15}$$

with

$$|\omega| = \left[(u_y - v_x)^2 + (v_z - w_y)^2 + (w_x - u_z)^2\right]^{1/2} \tag{16}$$

and the law-of-the-wall coordinate

$$y^+ = y(Re_{\text{lam}} \cdot \partial u/\partial y\,|_{\text{wall}})^{1/2} \tag{17}$$

In the other region

$$(Re_{\text{turb}})^{-1}_{\text{outer}} = KC_{cp}F_{\text{wake}}F_{\text{Kleb}} \tag{18}$$

$$F_{\text{wake}} = \min\left[C_{wk} \cdot (\Delta\tilde{V})^2 \cdot y_{\max}/F_{\max};\ y_{\max}F_{\max}\right] \tag{19}$$

where

$$\Delta\tilde{V} = (u^2 + v^2 + w^2)^{1/2}_{\max} - (u^2 + v^2 + w^2)^{1/2}_{\min}$$

and

$$F_{\max} = \max(|\omega|\ell/k),\ y_{\max} = y(F_{\max})$$

The constants are given in Ref. 16.

This algebraic turbulence model is implemented with three modifications to handle flows with massive transitional and fully turbulent crossflow separation.

First, consider the case of a transitional crossflow pattern. Following the ideas of Pulliam and Steger,[6] the crossflow is assumed to be laminar as long as it remains attached or it is just slightly separated. Once the flow is massively separated, it is assumed to be fully turbulent. Here, massive crossflow separation means that its radial extent exceeds the boundary-layer thickness, which is estimated by using the empirical formula for boundary-layer flow without pressure gradient over a flat plate:

$$\delta/\ell = 5.4\ Re_\ell^{-1/2} \tag{20}$$

where $\ell = \pi d/2$.

Figure 2 illustrates how the transition model is implemented. The solution is monitored in each crossplane by marching from the windward to the leeside meridian along a circumferential grid line a few step sizes off the body surface. Numbering the radial points with k ($k = 1$: body surface), the distance between circumferential grid line and body surface is given by $y_k > \delta/\ell$. The onset of massive crossflow separation is detected by the first occurrence of a negative product of two consecutive crossflow velocities.

The second modification is necessitated because the function $F(y)$ exhibits two relative extrema for flows with massive crossflows separation. The first maximum off the surface is associated with the attached boundary-layer-like flow, and it gives the appropriate value of the eddy viscosity. The second, larger extremum is due to the local extremum of vorticity in a shear layer, which rolls up into a primary vortex. When the second relative extremum of $F(y)$ is chosen, the eddy viscosity

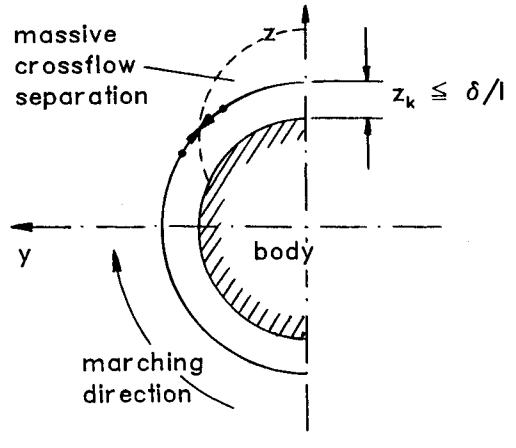

Fig. 2 Illustration of crossflow separation model including transition.

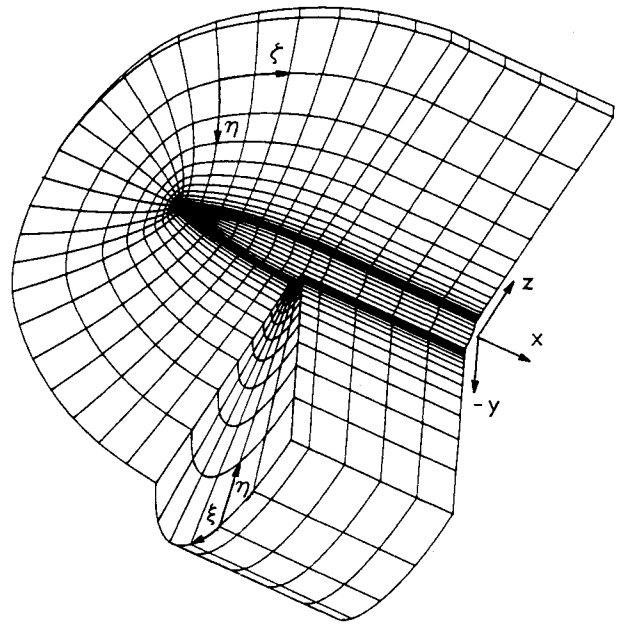

Fig. 3 Partial view of C-O-type grid around a 3.5-caliber, tangent-ogive cylinder.

in the outer region is grossly overpredicted. To select the correct $F_{\max}$, the solution is again monitored in each crossplane $i = \text{const}$. Starting from the windward meridian ($j = 1$), $F(y)$ is computed along each radial line (i,j) sweeping outboard. As Degani and Schiff,[9] we define $F_{\max} = F(y')$ when we encounter $F(y) < 0.9\,F(y')$ for $y > y'$. This logic correctly distinguishes between the two extrema of $F(y)$ as long as they are spaced far enough apart. This requirement is by definition satisfied for transitional crossflow separation patterns where the turbulence modeling sets in only after massive crossflow separation has been encountered. For fully turbulent crossflow separation patterns, this requirement can be violated in the vicinity of the primary separation, where the separated shear layer lies close to the outer edge of the attached boundary layer.

The third modification is used to correctly distinguish between the two relative extrema in $F(y)$ for fully turbulent crossflow in the neighborhood of a primary separation. One can either use the "cutoff" distance concept by Degani and Schiff[9] or the "switch" that is employed in modeling transitional crossflow separations. As long as there is no massive separation, the original version of the Baldwin-Lomax turbulence model is utilized. Once massive crossflow separation is encountered, which is detected by the switch (the first modification to the Baldwin-Lomax model), the second modification is invoked.

Transition in longitudinal direction is either handled in an ad hoc fashion (i.e., experimental data are used to determine transition), or some semiempirical concept, such as the Esch factor which approximates the effects of angle of attack on the streamline length,[20] is employed.

IV. Initial and Boundary Conditions

The initial procedure is to use uniform freestream flow everywhere except $u = v = w = 0$ along the body surface. The boundaries are treated explicitly. Freestream values are specified at the far-field boundaries except along the outflow boundary where a first-order extrapolation in combination with $p = \text{const} = 0$ is used. Assuming bilateral symmetry, reflection conditions are specified along the symmetry plane. On the body surface $u = v = w = 0$, and the pressure is computed from a limiting form of the Navier-Stokes equations taken at a solid surface

$$p_y = Re^{-1}v_{yy} \tag{21}$$

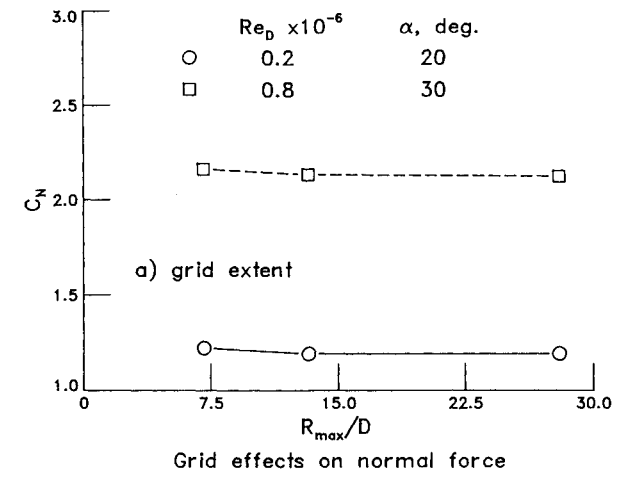

a)

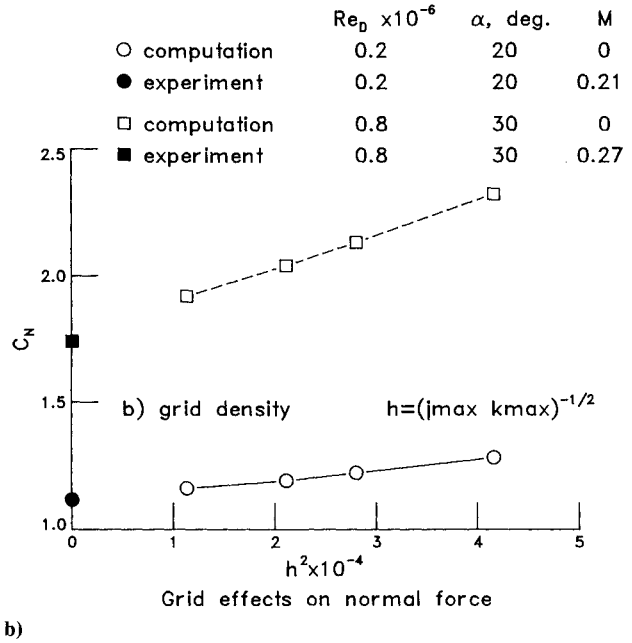

b)

Fig. 4 Grid effects on computed normal force.

with v and y assumed to be normal to the surface. Equation (21) is evaluated using second-order, accurate, finite-difference approximations. The limiters $\phi^{\pm}_{m,\ell}$ ($\ell = i, j$, or k) and ΔQ^n are set to zero along all boundaries leading to first-order accuracy at the boundaries.

V. Results

Solutions are shown for vortical flows ($Re = 0.2$, 0.8, and 3.0 million) over a 3.5-caliber tangent-ogive cylinder at 20 and 30 deg angle of attack. All calculations are carried out with the assumption of bilateral symmetry of the flow. This assumption, as it will be shown, is fully justified for $\alpha = 20$ deg. For $\alpha = 30$ deg, the onset of vortex asymmetries have experimentally been observed for $x/D \geq 4.0$ ($x/D = 0.0$: body apex), that is over the cylindrical portion of the subject geometry. Thus, for $\alpha = 30$ deg, a good agreement between the present computations and experiments can only be expected for $x/D < 4.0$.

The tangent-ogive cylinder is illustrated by the perspective view of a C-O-type grid in Fig. 3. These grids are generated by rotating a C-type grid around the longitudinal body axis. The C-type grid is computed in, say, the symmetry plane as a solution to an elliptic system.[21] The radial lines are equiangularly spaced. The radial stretching is computed from a geometric progression,[22] and it was limited by

$$\ell n(\Delta y_k / \Delta y_{k-1}) \cdot k_{\max} \leq 7 \tag{22}$$

That limitation in combination with the number of circumferential points varying between 49 and 121 keeps the order of the cell aspect ratio in cross planes below 10. Neglecting the rather small longitudinal pressure variation and considering cells adjacent to both the symmetry plane and body surface, the cell aspect ratio is proportional to the ratio of the radial and circumferential velocity components for incompressible flow. The cell aspect ratio can be manipulated by radial stretching and/or a circumferential clustering as, for instance, proposed by Yates and Chapman.[22] Compressing the cell radially too much by either one or both means caused overprediction (underprediction) of surface pressure and skin friction along the windward (leeward) side of the forebody.

Figures 4 show the effects of cross-sectional grid extent and grid resolution on normal force. The baseline grid in Fig. 4a consists of $40 \times 73 \times 65$ grid points, and its far-field boundary is located at $R_{\max}/D = 28$. Retaining the same grid density, the computational domains of lesser extent are obtained by dropping radial points in the far field (i.e., $R_{\max}/D = 13.22$ corresponds to a $40 \times 73 \times 58$ grid, etc.). In Fig. 4b, a second-order accurate convergence of the normal force is apparent when correlated with the representative step size $h = (j_{\max} \cdot k_{\max})^{-1/2}$. This quasi-two-dimensional approach in the grid effect study was chosen after having varied the number of crossplanes from 40 to 150 without detecting any discernible changes in the loads or in the flow details like surface pressure distribution. The length of the circular cylinder has been changed between 7 and 35 base diameters. For the afterbody exceeding $x/D = 20$, difficulties are encountered in converging our solutions to a stable, steady state. Two sources for this problem were identified: 1) unsteady vortex shedding along the afterbody and 2) an insufficient resolution of these body vortices because of the longitudinal stretching of the grid.

Figures 5 gives a convergence summary for the four cases considered in Fig. 4b. It is seen that the L_2 norms of all residuals exhibit a limit-cycle behavior after they have dropped about two and one-half orders of magnitude within about 400 iterations. This behavior is attributed to a "subscale" unsteadiness near the primary separation, which fluctuated by about ± 1 grid points in the circumferential direction. Since the subscale unsteadiness had little to no impact on global properties such as lift and pitching moment as well as local quantities such as surface pressure, the solutions in Fig.

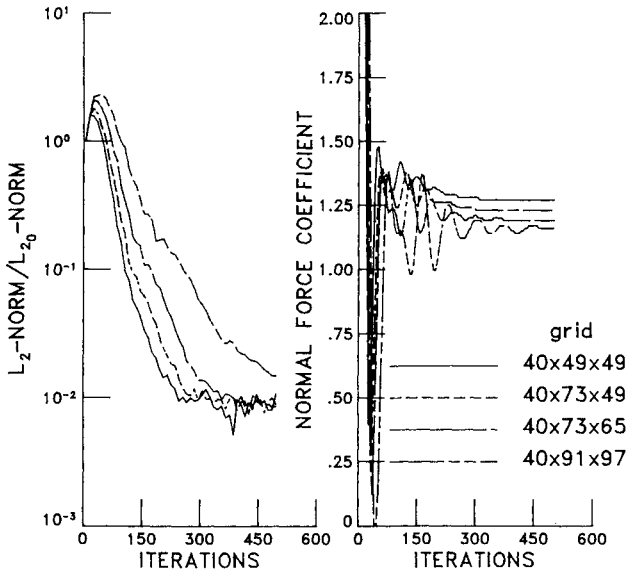

Fig. 5 Convergence summary: $\alpha = 20$ deg, $Re_D = 0.2$ million, CFL = 10.

4 are considered to be fully converged from an engineering point of view. The convergence summary in Fig. 5 is representative of all test cases considered. The CPU time per grid point and per iteration is about 29 and 38 μs on a CDC Cyber 205 and a Cray Y-MP supercomputer, respectively.

Figure 6 shows comparisons of measured (Dr. Lewis B. Schiff of NASA Ames Research Center provided us with the experimental data that Dr. Peter J. Lamont took while working as an NRC Postdoctoral Research Associate at Ames. Comparison with related experimental data[23] and theoretical results[5] convinced us that there is a pressure offset of about 1.3 psf in Lamont's data. The corrected data is shown.) and computed surface pressure coefficients for four axial stations: $x/D = 0.5$, 2, 3.5, and 6. The flow parameters are $\alpha = 20$ deg and $Re_D = 0.2$ million.

The wind tunnel model has 36 equiangularly spaced orifices at 12 cross stations which are evenly distributed for $0.5 \le x/D \le 6.0$. To assess the effects of roll orientation, the model was rolled in increments of $\Delta\theta = 30$ deg. For $\alpha = 30$ deg, a roll orientation of nominally 240 degrees was found to produce minimum overall side force for the Reynolds numbers in the present study. In order to avoid issues related to the variation of roll angle, this roll orientation was retained for the comparison in Fig. 6.

The calculations are carried out on a $40 \times 73 \times 65$ grid. The surface computed surface pressures for $0 \text{ deg} \le \theta \le 180$ deg are directly taken from the numerical solution; for $180 \text{ deg} \le \theta \le 360$ they are obtained through mirror imaging.

For $x/D < 3.5$, the flow is apparently laminar, and both calculations match the experimental data quite well. For $x/D \ge 3.5$, the laminar computation clearly overpredicts the influence of the primary vortices in the surface pressure distribution and locates their respective positions too far away from the leeside wind plane. In the computation with the present transition model, the positions of the primary vortices are less than 5 deg off, their suction is of comparable strength, and the effects of something like laminar separation bubbles on the equatorial C_p distributions can be clearly seen. In this calculation, the flow is assumed to be laminar unless massive crossflow separation is encountered for $x/D > 3.0$, where the modifications to the Baldwin-Lomax turbulence model are invoked as described in Sec. III.

The computed surface pressure distributions in Fig. 6 differ somewhat from previously[10,24] published results for this flow case. Compared to the calculations in Ref. 10, the radial grid stretching in the present computations has been slightly relaxed to satisfy the constraint imposed by Eq. (22). In Ref. 24, reducing the parameter β from 1.0 to 0.1 helped to better

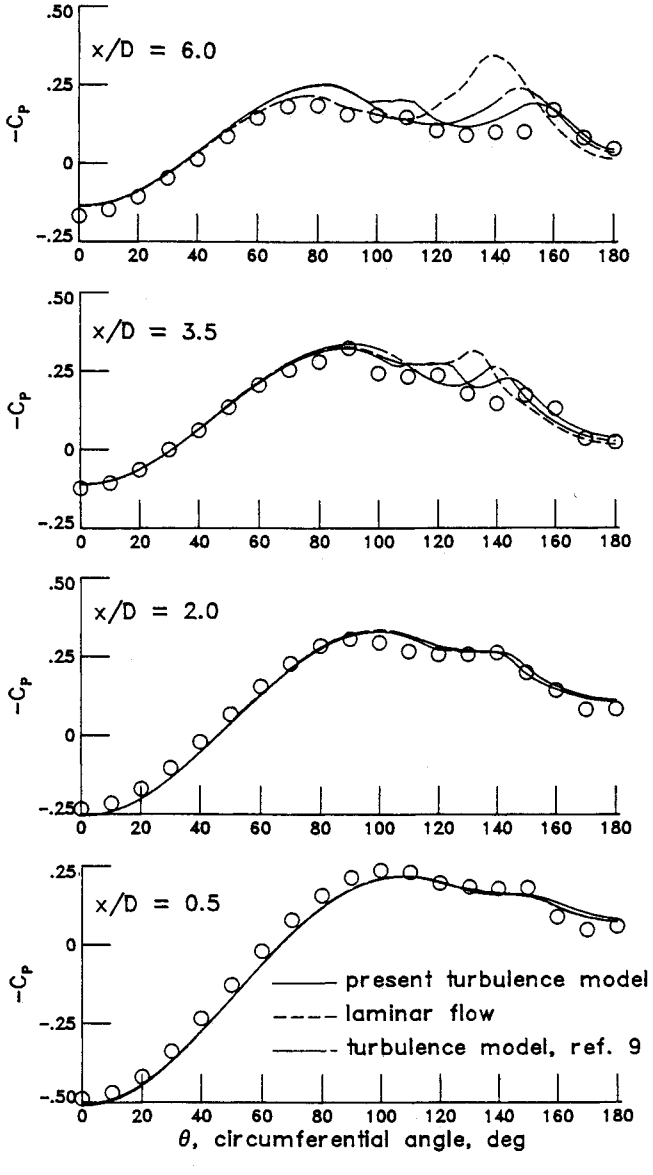

Fig. 6 Experimental (symbols) and computational (lines) circumferential surface pressure distributions: $\alpha = 20$ deg, $Re_D = 0.2$ million, $40 \times 73 \times 65$ grid points.

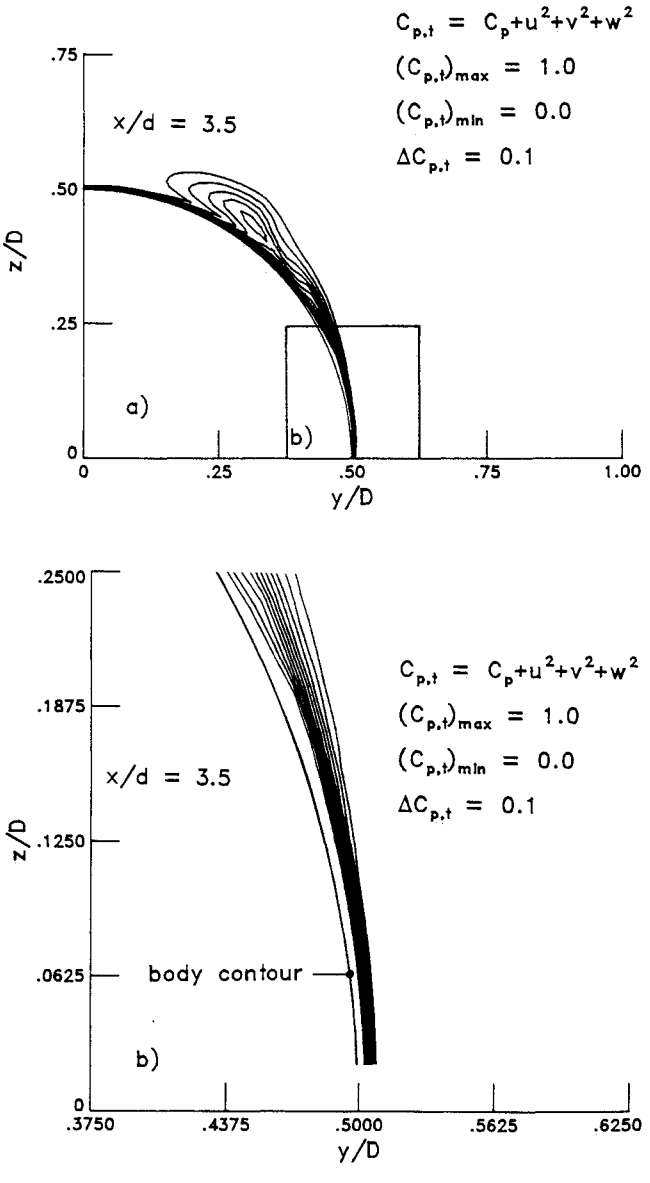

Fig. 7 Computed crossflow separation, pattern-total pressure contours: $\alpha = 20$ deg, $Re_D = 0.2$ million, $40 \times 73 \times 65$ grid points.

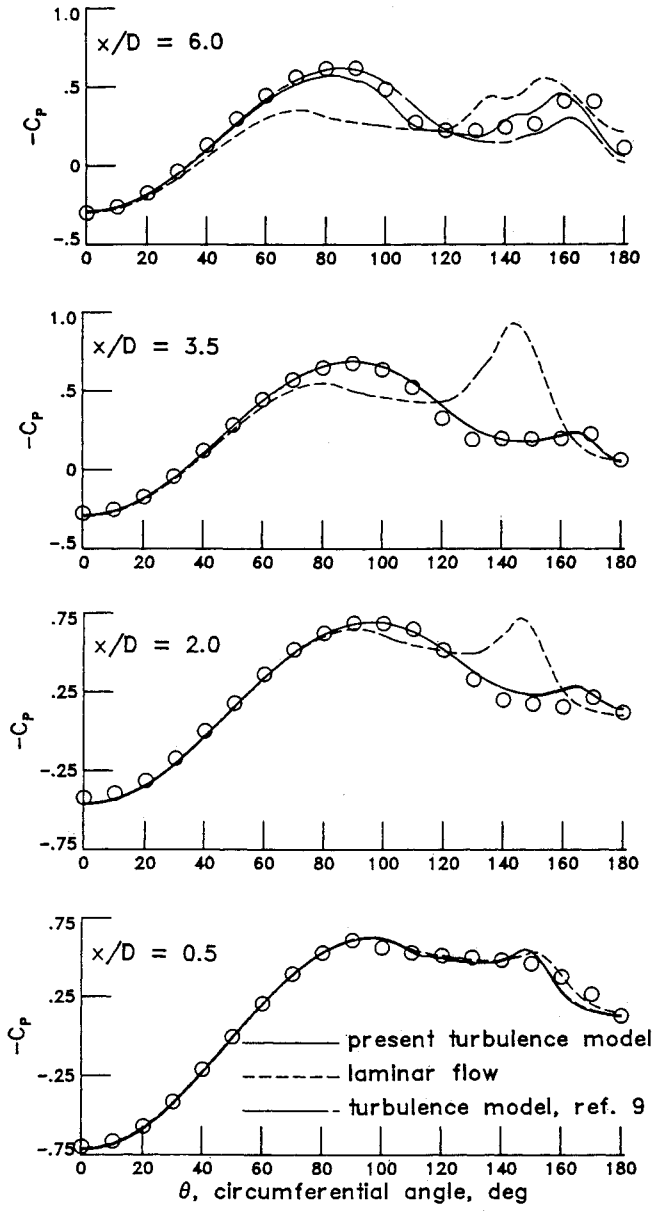

Fig. 8 Measured (symbols) and computed (lines) circumferential surface pressure distributions: $\alpha = 30$ deg, $Re_D = 0.8$ million, $40 \times 73 \times 65$ grid points.

match the experimental pressure data in the windward and equatorial portions of the body. However, additional studies on the dependency of the results on the parameter β for other flow cases reported here and in an extension of this study to asymmetric flows[25] demonstrated that this "improvement" was an isolated case and thus fortuitous.

Further evidence of the existence of the bubble-like crossflow pattern in the equatorial region is given in Fig. 7, which shows total pressure contours in a crossplane at $x/D = 3.5$. The blank area between ogive surface and $C_{p,t}$ contours in Fig. 7b shows the thickening and thinning of the boundary layer. That reduces the effective curvature of the body surface and results in the formation of a pressure plateau. From crossflow-velocity vector plots (not shown here), it is known that the blank area corresponds to a flat separation bubble. The reduction in radial extent of the mild separation within the boundary layer is because of a local acceleration of the flow in the neighborhood of the regime where the flow actually lifts off the surface. The local acceleration, in turn, is caused by entrainment effects of the flow induced by the separated shear layer.

Using the same layout as in Fig. 6, Fig. 8 shows comparisons of computed surface pressures with Lamont's data for $\alpha = 30$ deg and $Re_D = 0.8$ million.

The labelling with Method (A) and (B) refers to the different approaches to invoke the modifications to the Baldwin-Lomax turbulence model to simulate fully turbulent crossflow separations. Method (A) designates the "switch" approach as described in Sec. III and Method (B) the "cutoff distance" concept by Degani and Schiff.[9]

In both calculations, the flow has been assumed to be laminar for $x/D \leq 1.5$, and fully turbulent for $x/D > 1.5$. Both calculations match the experimental surface pressure data quite closely for $x/D \leq 3.5$. For $x/D > 3.5$, the assumption of bilateral symmetry becomes decreasingly valid as exemplified by the most severe mismatch between computations and experiment at $x/D = 6.0$.

The results with the "switch" approach (method (A)) are obtained as described in Sec. III. Varying the parameter δ/l in Eq. (20) by $\pm 50\%$ had little impact on the results obtained with method (A). For method (B), the results showed some sensitivity towards choices for the constant c in the equation comprising the cutoff distance concept by Degani and Schiff (see Ref. 9, p. 185). The published value of c (i.e., 1.5) for fully turbulent flows was found to produce unacceptable results for this transitional flow application.[24] A value of 6 for c was used for the results in Fig. 8.

Figure 9 shows a comparison of computational and experimental (sketched after Keener[2]) surface flow patterns. The lines indicating primary separation are in good agreement. The top views show two distinct regimes in which the surface streamlines appear to collocate. Keener[2] interpreted these regimes as primary and secondary separation lines along which the flow lifts off to form a primary and a secondary vortex, respectively. Because both experimental and computational surface-flow pictures neither reveal the usual fishbone structure along the collocated lines nor a reattachment line between them, the computed flowfield results were analyzed further using computer graphics.

Figure 10 shows a computational surface flow over the tangent-ogive cylinder and two superimposed cross-sectional streakline patterns. The surface flow indicates a reattachment

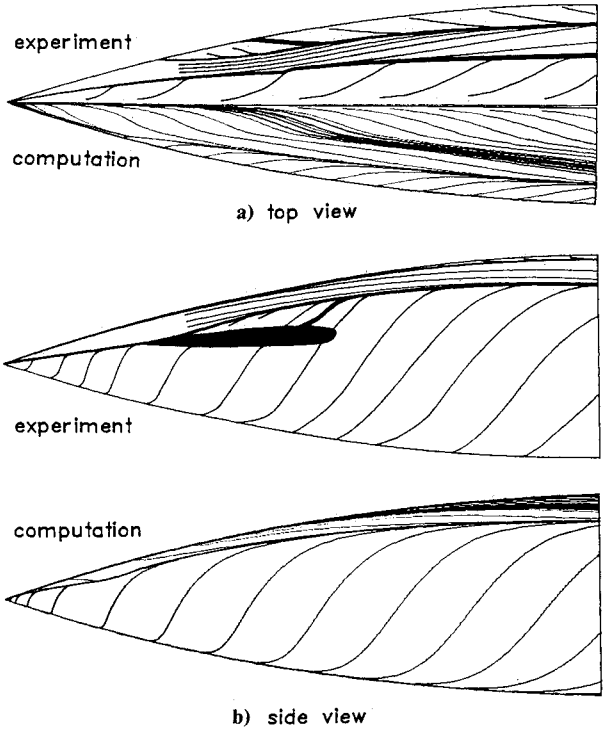

Fig. 9 Surface flow patterns: $\alpha = 20$ deg, $Re_D = 0.8$ million, $40 \times 91 \times 97$ grid points.

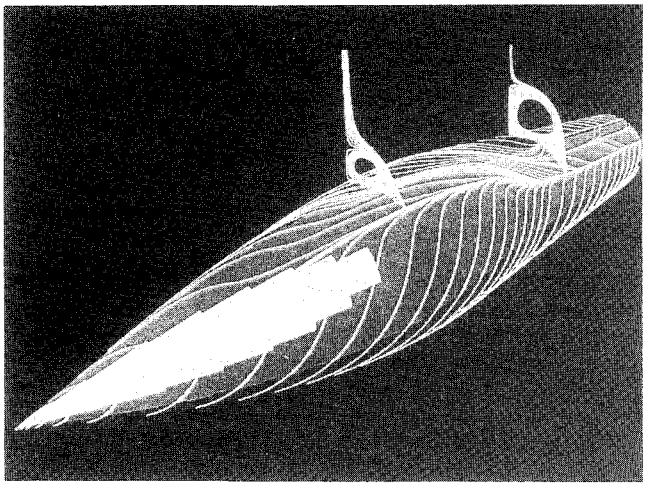

Fig. 10 Particle traces on surface and in crossplanes: $\alpha = 30$ deg, $Re_D = 0.8$ million, $40 \times 91 \times 97$ grid points.

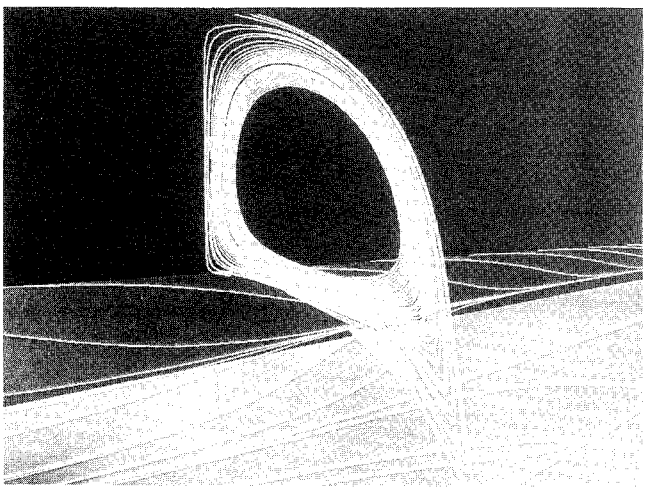

Fig. 12 Particle traces in crossplanes at $x/D = 4$: $\alpha = 30$ deg, $Re_D = 0.8$ million, $40 \times 91 \times 97$ grid points.

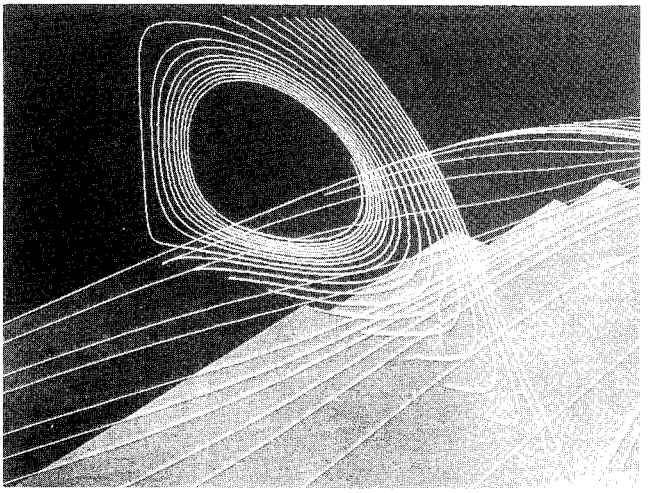

Fig. 11 Particle traces in crossplane at $x/D = 2$, $\alpha = 30$ deg, $Re_D = 0.8$ million, $40 \times 91 \times 97$ grid points.

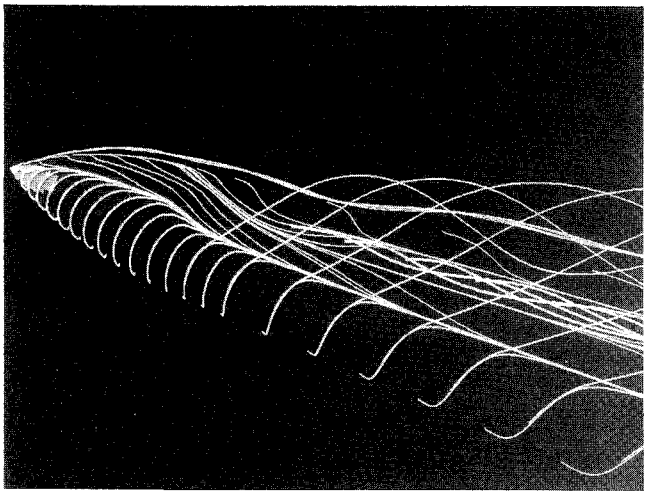

Fig. 13 Primary separtion as indicated by surface flow and off-body particle traces: $\alpha = 30$ deg, $Re_D = 0.8$ million, $40 \times 91 \times 97$ grid points.

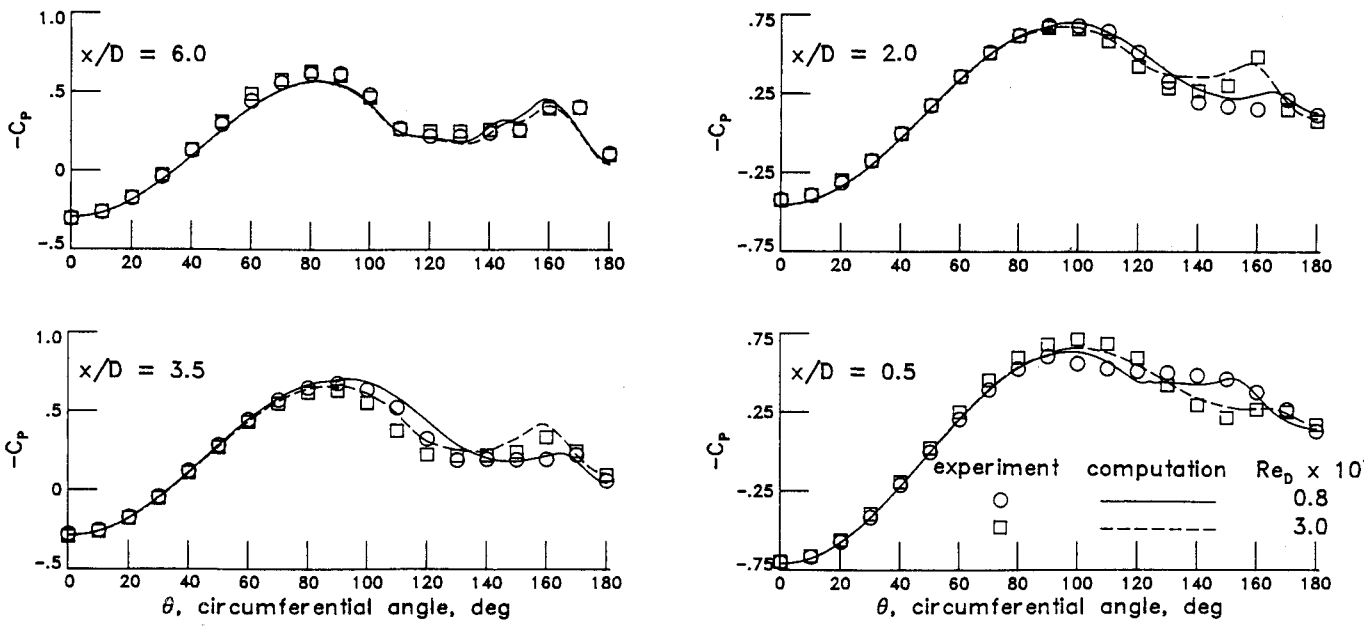

Fig. 14 Measurement and computed circumferential pressure distributions: $\alpha = 30$ deg, $40 \times 91 \times 97$ grid points.

line between the two separation lines only along the cylindrical section of the body. This reattachment line emanates from the symmetry plane at about the junction between the tangent ogive and cylinder. Enlarging the two cross-sectional streakline patterns (see Figs. 11 and 12) demonstrates that while there is no secondary vortex over the tangent ogive (see Fig. 11), a clearly developed secondary vortex exists above the cylinder (see Fig. 12). Over the tangent ogive, the flow coming from the windward and leeside meridional regions appears to be separated by flow that simultaneously "barrels through" and lifts off. Further analysis of the flowfield results using computational flow visualization techniques revealed that the flow forming the primary vortex separates at a considerably lower circumferential angle than suggested by the line that is usually referred to as the primary separation line (see Fig. 13). This result supports a major finding in a related computational study on flows over tangent-ogive cylinders by Yates and Chapman.[22] (Comparisons with flow visualization studies on flowfield results computed on an $80\times121\times129$ grid indicated that the results shown here are spatially fully converged.)

The Reynolds number effects were found to diminish for $Re_D > 1$ million. This is exemplified by the comparisons of computational and experimental surface pressure distributions in Fig. 14. In the calculations, the flow is assumed to be fully turbulent for $x/D > 1.5$ for $Re_D = 0.8$ million and for $x/D > 0.125$ for $Re_D = 3.0$ million. The differences between the C_p distributions for $Re_D = 0.8$ million and $Re_D = 3.0$ million have diminished for $x/D = 3.5$ and are almost indiscernible for $x/D = 6$. This holds true for both experiment and computation despite the decreasing validity of the assumption of bilateral symmetry for $x/D > 3.5$. A surge of the suction underneath the primary vortex in the intermediate stations (e.g., $x/D = 2$) is observed in the computation as well as in the experiment. This phenomenon is attributed to differences in the separation angle for the two Reynolds-number cases. For the $Re_D = 3.0$ million case, the flow separates at a circumferential angle of about 130 deg (typical for fully turbulent flow over an expanding nose); whereas, for $Re_D = 0.8$ million, the flow remains attached until about 140 to 150 deg (typical for a transitional flow). The earlier separation leads to a higher velocity in the region of separation that translates into an increase in the vorticity shed which, in turn, causes a stronger suction.

VI. Conclusions

A proven, incompressible Navier-Stokes solver has been employed to study the effects of Reynolds number and angle of attack on low-speed flows with massive crossflow separations over a 3.5-caliber, tangent-ogive cylinder. A rational extension of the Baldwin-Lomax turbulence model has been introduced that 1) has the capability to simulate transitional crossflow separation and 2) appears to accurately and dependably predict values for the eddy viscosity in the vicinity of the primary separation for fully turbulent crossflow separation. The computed flowfield results are in good agreement with experimental data. As in an earlier experiment, the present computations show that the Reynolds number effects at moderate angles of attack ($\alpha \le 30$ deg) diminish for $Re_D > 1$.

Acknowledgments

NASA Langley Research Center sponsored the work of the first author under NASA Contract NAS1-17919. The contributions by Michael J. Hemsch in many fruitful discussions are also gratefully acknowledged.

References

[1]Hemsch, M. J. and Nielsen, J. N. (eds.), *Progress in Astronautics and Aeronautics: Tactical Missile Aerodynamics*, Vol. 104, AIAA, New York, 1986.

[2]Keener, E. R., "Oil Separation Patterns on an Ogive Forebody," *AIAA Journal*, Vol. 21, No. 4, April 1983, pp. 550–556.

[3]Tobak, M., and Peake, D. J., "Topology of Three-Dimensional Separated Flows," *Annual Review of Fluid Mechanics*, Vol. 14, 1982, pp. 61–86.

[4]Angelucci, S. B., "A Multivortex Method for Axisymmetric Bodies at Angles of Attack," *Journal of Aircraft*, Vol. 8, No. 12, Dec. 1971, pp. 959–966.

[5]Mendenhall, M. R., and Lesieutre, D. J., "Prediction of Vortex Shedding from Circular and Noncircular Bodies in Subsonic Flow," NASA CR-4037, Jan. 1987.

[6]Pulliam, T. H., and Steger, J. L., "On Implicit Finite-Difference Simulations of Three-Dimensional Flow," AIAA Paper 78-10, Jan. 1978.

[7]Klopfer, G. H., and Nielsen, J. N., "Computational Fluid Dynamic Applications to Missile Aerodynamics," Paper No. 3, AGARD CP-336, Sept. 1982.

[8]Wardlaw, A. B., Jr., Solomon, J. M., and Baltakis, F. P., *Progress in Astronautics and Aeronautics: Tactical Missile Aerodynamics*, Vol. 104, edited by M. J. Hemsch, and J. N. Nielsen, AIAA, New York, 1986, pp. 669–722.

[9]Degani, D., and Schiff, L. B., "Computation of Turbulent Supersonic Flows Around Pointed Bodies Having Crossflow Separation," *Journal of Computational Physics*, Vol. 66, No. 1, Sept. 1986, pp. 173–196.

[10]Hartwich, P.-M., Hsu, C.-H., Luckring, J. M., and Liu, C. H., "Aerodynamic Applications of an Efficient Incompressible Navier-Stokes Solver," International Council of the Aeronautical Sciences, ICAS Paper 88-5.9.1, Aug. 1988.

[11]Hartwich, P.-M., Hsu, C.-H., and Liu, C. H., "Vectorizable Implicit Algorithms for the Flux-Difference Split, Three-Dimensional Navier-Stokes Equations," *ASME Journal of Fluids Engineering*, Vol. 110, No. 3, Sept. 1988, pp. 297–305.

[12]Hartwich, P.-M., and Hsu, C.-H., "High Resolution Upwind Schemes for the Three-Dimensional, Incompressible Navier-Stokes Equations," *AIAA Journal*, Vol. 26, No. 11, Nov. 1988, pp. 1321–1328.

[13]Lamont, P. J., "The Effect of Reynolds Number on Normal and Side Forces on Ogive Cylinders at High Incidence," AIAA Paper 85-1799, Aug. 1985.

[14]Ward, K. C., and Katz, J., "Boundary-Layer Separation and the Vortex Structures Around an Inclined Body of Revolution," AIAA Paper 87-2276-CP, Aug. 1988.

[15]Steger, J. L., and Kutler, P., "Implicit Finite-Difference Procedures for the Computation of Vortex Wakes," *AIAA Journal*, Vol. 15, April 1977, pp. 581–590.

[16]Baldwin, B. S., and Lomax, H., "Thin-Layer Approximation and Algebraic Turbulence Model for Separated Turbulent Flows," AIAA Paper 78-257, Jan. 1978.

[17]Thomas, J. L., and Walters, R. W., "Upwind Relaxation Algorithms for the Navier-Stokes Equations," *AIAA Journal*, Vol. 25, April 1987, pp. 527–534.

[18]Chorin, A. J., "A Numerical Method for Solving Incompressible Viscous Flow Problems," *Journal of Computational Physics*, Vol. 2, No. 1, Aug. 1967, pp. 12–26.

[19]Steger, J. L., "Implicit Finite-Difference Simulation of Flow about Arbitrary Two-Dimensional Geometries," *AIAA Journal*, Vol. 16, July 1978, pp. 679–686.

[20]Polhamus, E. C., "A Review of Some Reynolds Number Effects Related to Bodies at High Angles of Attack," NASA CR-3809, Aug. 1984.

[21]Hartwich, P.-M., "Three-Dimensional Grids as Solutions of Elliptic Systems," AIAA Paper 86-0430, Jan. 1986.

[22]Yates, L. A., and Chapman, G. T., "A Numerical Investigation of Crossflow Separation on a Three-Caliber Tangent-Ogive Cylinder," *AIAA Journal*, Vol. 26, Oct. 1988, pp. 1223–1230.

[23]Champigny, P. G., "Reynolds Number Effect on the Aerodynamic Characteristics of an Ogive-Cylinder at High Angles of Attack," AIAA Paper 84-2176, Aug. 1984.

[24]Hartwich, P.-M., and Hall, R. M., "Navier-Stokes Solutions for Vortical Flows Over a Tangent-Ogive Cylinder," AIAA Paper 89-0337, Jan. 1989.

[25]Hartwich, P. M., Hall, R. M., and Hemsch, M. J., "Navier-Stokes Computations of Vortex Asymmetries Controlled by Small Surface Imperfections," AIAA Paper 90-0385, Jan. 1990.